RSC Advances

PAPER

View Article Online
View Journal | View Issue

Cite this: *RSC Adv.*, 2018, **8**, 35271

Significantly enhanced photoluminescence and thermal stability of $La_3Si_8N_{11}O_4:Ce^{3+},Tb^{3+}$ *via* the $Ce^{3+} \rightarrow Tb^{3+}$ energy transfer: a blue-green phosphor for ultraviolet LEDs†

Hui-Bing Xu,[ac] Wei-Dong Zhuang,*[a] Rong-Hui Liu,*[a] Yuan-Hong Liu,[a] Tian-Liang Zhou,[b] Yujin Cho,[c] Wei Gao,[a] Chun-Pei Yan,[a] Naoto Hirosaki[c] and Rong-Jun Xie*[b]

Received 21st August 2018
Accepted 21st September 2018

DOI: 10.1039/c8ra07011c

rsc.li/rsc-advances

A series of Ce^{3+}-, Tb^{3+}- and Ce^{3+}/Tb^{3+}-doped $La_3Si_8N_{11}O_4$ phosphors were synthesized by gas-pressure sintering (GPS). The energy transfer between Ce^{3+} and Tb^{3+} occurred in the co-doped samples, leading to a tunable emission color from blue to green under the 360 nm excitation. The energy transfer mechanism was controlled by the dipole–dipole interaction. The Ce^{3+}/Tb^{3+} co-doped sample had an external quantum efficiency of 46.7%, about 5.6 times higher than the Tb-doped $La_3Si_8N_{11}O_4$ phosphor (8.3%). The thermal quenching of the Tb^{3+} emission in $La_3Si_8N_{11}O_4$:Tb,Ce was greatly reduced from 74 to 30% at 250 °C, owing to the energy transfer from Ce^{3+} to Tb^{3+}. The blue-green $La_3Si_8N_{11}O_4$:0.01Ce,0.05Tb phosphor was testified to fabricate a warm white LED that showed a high color rendering index of 90.2 and a correlated color temperature of 3570 K. The results suggested that the co-doped $La_3Si_8N_{11}O_4$:Ce,Tb phosphor could be a potential blue-green down-conversion luminescent material for use in UV-LED pumped wLEDs.

1 Introduction

In recent years, white light-emitting diodes (w-LEDs) have drawn much attention due to their advantages over conventional lighting technologies, such as high efficiency, energy saving, environmental friendliness, compactness and longevity.[1–10] There are two common approaches to generate white light from LEDs.[11–13] The first one is to combine monochromatic blue, green and red LED chips to create white light. This method allows the production of high luminous efficacy but it also requires a complicated feedback electronic control which limits its application. The second one is to pump phosphor(s) with a blue, UV or near-UV LED chip (also called phosphor-converted w-LEDs), which promises cost effectiveness and ease of fabrication. Compared to the dichromatic wLEDs using the combination of a blue LED chip and a yellow-emitting phosphor (*e.g.*, YAG:Ce^{3+}), multi-phosphor-converted wLEDs driven by an UV LED chip enable to provide a super-high color rendering index (CRI > 90) and the excellent quality of light that can be widely used in supermarkets, surgical operations, museums, *etc.*[14–20] To realize this, highly efficient and thermally stable red, green and blue phosphors that can be excited by UV light are required.[21–24]

To develop green or green-to-blue emitting phosphors for such applications, one of the strategies is to co-dope Ce^{3+} and Tb^{3+} in one phosphor host, and to apply the energy transfer between Ce^{3+} and Tb^{3+} to realize the tunable color and enhanced photoluminescence properties.[25–28] For example, Wang *et al.* reported a novel blue-green emitting phosphor $NaBaScSi_2O_7:Ce^{3+},Tb^{3+}$ with an internal quantum efficiency (IQE) of 36%.[29] Xiao *et al.* addressed that the green emission of Tb^{3+} in $Ba_2Y_5B_5O_{17}:Ce^{3+},Tb^{3+}$ at 423 K could remain 92% of its intensity at room temperature.[30] Du *et al.* found that in the blue-green emitting phosphor $LaSi_3N_5$:0.09Ce^{3+},0.12Tb^{3+} the Tb^{3+} luminescence had a higher thermal stability than the Ce^{3+} luminescence at 423 K (~90% *vs.* ~70% of the initial luminescence).[31] Zhang *et al.* investigated the green phosphor LaOBr:Ce^{3+},Tb^{3+}, and observed that the green emission at 433 K could maintain 90–100% of its intensity at room-temperature.[32]

Among the huge number of luminescent materials for wLEDs, the rare-earth doped (oxy)nitride phosphors have drawn much attention due to their abundant emission color, high

[a]*National Engineering Research Center for Rare Earth Materials, General Research Institute for Nonferrous Metals, Grirem Advanced Materials Co., Ltd., Beijing 100088, People's Republic of China. E-mail: wdzhuang@126.com; griremlrh@126.com*

[b]*College of Materials, Xiamen University, Xiamen, Fujian 361005, People's Republic of China. E-mail: rjxie@xmu.edu.cn*

[c]*Sialon Group, National Institute for Materials Science, 1-1 Namiki, Tsukuba, 305-0044, Japan*

† Electronic supplementary information (ESI) available: Ionic radii (Å) of La^{3+}, Ce^{3+}, Tb^{3+} for the given coordination number (CN) (Table S1) and EDS spectrum of $La_3Si_8N_{11}O_4$:0.01Ce,0.2Tb (Fig. S1). See DOI: 10.1039/c8ra07011c

conversion efficiency and small thermal quenching.[33–45] Eu^{2+} and Ce^{3+} are the mostly used activators in (oxy)nitride phosphors, leading to a variety of interesting luminescent materials for white LEDs, such as α-sialon:Eu^{2+}, β-sialon:Eu^{2+}, $CaAlSiN_3$:Eu^{2+}, $Sr[LiAl_3N_4]$:Eu^{2+}, $La_3Si_6N_{11}$:Ce^{3+}, and *etc.*[46–50] On the other hand, to the best of our knowledge, there are very limited investigations on co-doped (oxy)nitride phosphors. Liu *et al.* reported the greatly enhanced luminescence in γ-alon:Mn^{2+} by co-doping Eu^{2+}, which enables to a promising green phosphor for near-UV LEDs.[51] Song *et al.* realized the tunable emission colors in Eu^{2+} and Ce^{3+} co-doped $SrSi_2O_2N_2$ *via* the energy transfer between Eu^{2+} and Ce^{3+}.[52] Therefore, it has great opportunities to develop (oxy)nitride phosphors with enhanced photoluminescence properties by realizing the efficient energy transfer in them.

$La_3Si_8N_{11}O_4$ is a good host for Ce^{3+} or Eu^{2+} that has intense blue emissions under the UV excitation.[3,53] Moreover, $La_3Si_8N_{11}O_4$:Ce^{3+} also shows smaller thermal quenching than other phosphors in system La–Si–N–O–Ce.[54] In this work, we attempt to investigate the photoluminescence of Ce^{3+} and Tb^{3+} co-doped $La_3Si_8N_{11}O_4$, and to apply the energy transfer strategy to enhance photoluminescence properties of $La_3Si_8N_{11}O_4$:Ce^{3+},Tb^{3+}. The photoluminescence properties and the energy transfer mechanism of the co-doped materials will be investigated and discussed.

2 Experimental

A series of Ce^{3+}-, Tb^{3+}-, and Ce^{3+}/Tb^{3+}-doped $La_3Si_8N_{11}O_4$ ($La_3Si_8N_{11}O_4$:*y*Ce, *x*Tb, $y = 0$–0.15, $x = 0$–0.30) powder samples were synthesized *via* the high temperature solid-state reaction method. α-Si_3N_4 (SN-E10, Ube Industries, Tokyo, Japan), LaN (laboratory made), La_2O_3 (Shin-Etsu Chemical Co., Tokyo, Japan), CeN (laboratory made) and TbN (laboratory made) were thoroughly mixed with mortar and pestle for 15 min in a nitrogen-field glovebox (H_2O < 1 ppm, O_2 < 1 ppm). The powders were put into BN crucibles and fired at 1800 °C for 2 h under 1.0 MPa nitrogen atmosphere. After firing, the samples were gradually cooled to room temperature in the furnace under the N_2 protection. Finally, the fired powders were finely ground using a mortar for further measurements.

The crystalline phase of the synthesized samples was collected on an X-ray diffraction (XRD, Smart Lab, Rigaku, Tokyo, Japan) operating at 40 kV and 40 mA and using Cuα_1 radiation ($\lambda = 1.54056$ Å). A step size of 0.02° with a scan speed of 10° per minute over the 2θ range 5–80°.

Energy-dispersive X-ray spectroscopy (EDS) and mapping measurements of the cross-section particles were carried out at room temperature with a Hitachi SU-8000 scanning microscope at an accelerating voltage of 5 kV. SEM and cathodoluminescence (CL) measurements were performed using a field emission scanning electron microscope (SEM, Hitachi S4300, Tokyo, Japan) equipped with a CL system (Horiba MP32S/M, Horiba, Tokyo, Japan).

High-resolution transmission electron microscopy (TEM) images and the EDS mapping were recorded using a JEM-3100FEF electron microscope (JEOL, Tokyo, Japan) fitted with the field emission gun at accelerating voltage of 300 kV.

Photoluminescence spectra at room temperature were analyzed with a Hitachi F-4500 spectrophotometer equipped with a Xe lamp. The diffuse reflectance spectra were measured with a UV-vis spectrophotometer (Ubest V560, Jasco, Tokyo, Japan), using a Spectralon diffusive white standard for calibration.

The fluorescence lifetime measurement was taken on a time-correlated single-photon counting fluorometer (TemPro, Horiba Jobin-Yvon, Tokyo, Japan) equipped with a NanoLED-370 nm with a pulse duration full width at half-maximum of ~1 ns.

The temperature-dependent photoluminescence was measured in the range of 25–250 °C with a multichannel Photal MCPD-7000 detector, using a Xe lamp as an excitation source. The quantum efficiency (QE) measurements were done using a multichannel spectrometer (MCPD-7000, Otsuka Electronics, Tokyo, Japan), with a Xe lamp as an excitation source, and the $^{@}BaSiO_4$ white standard was used for calibration. The external (η_0) and internal (η_i) QEs were calculated according to the following equations:[55]

$$\eta_0 = \frac{\int \lambda P(\lambda)\mathrm{d}\lambda}{\int \lambda E(\lambda)\mathrm{d}\lambda}$$

$$\eta_i = \frac{\int \lambda P(\lambda)\mathrm{d}\lambda}{\int \lambda\{E(\lambda) - R(\lambda)\}\mathrm{d}\lambda}$$

where $E(\lambda)/h\nu$, $E(\lambda)/h\nu$ and $E(\lambda)/h\nu$ are the number of photons in the excitation, reflectance and emission spectra of the phosphor sample, respectively.

A white LED was fabricated by using a UV-LED chip (365 nm) and $La_3Si_8N_{11}O_4$:0.01Ce,0.05Tb (blue-green), $SrSi_2N_2O_2$:Eu (green) and $Sr_2Si_5N_8$:Eu (red) phosphors. The optical properties of the white LED were measured using an integrated sphere spectroradiometer system (LHS-1000, Everfine Co., Hangzhou, China). The operated current and voltage were 300 mA and 3.756 V, respectively.

3 Results and discussion

3.1 Phase identification

The XRD patterns of $La_3Si_8N_{11}O_4$:1%Ce,*x*Tb doped with varying Tb^{3+} concentrations ($x = 0$–0.3) are shown in Fig. 1. All the diffraction peaks of the selected samples agree well with the standard data of $La_3Si_8N_{11}O_4$ (JCPDS card #48-1597), and no impurity phase is identified. It indicates that the doping of Ce and Tb does not change the phase purity of the $La_3Si_8N_{11}O_4$ host. Moreover, the lattice parameters of samples decrease with increasing the Tb concentration (*x*), as seen in Fig. 2. As reported by Grins *et al.*, $La_3Si_8N_{11}O_4$ has two different La sites, with La1 being coordinated by 4 O/N and 2 O atoms and La2 atom coordinated by 5 O/N, 2 O and 1 N atoms (Fig. 1b).[56] According to the effective ionic radius of cations with varying coordination numbers (CN), the radius of both Ce^{3+} and Tb^{3+} is smaller than that of La^{3+}, as is listed in Table S1.†[57] Therefore,

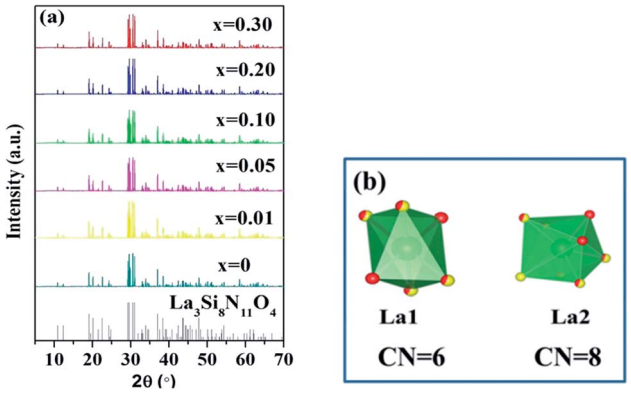

Fig. 1 XRD patterns of (a) $La_3Si_8N_{11}O_4$:0.01Ce,*x*Tb ($x = 0-0.3$) and (b) the coordination environment of La1 and La2 in the $La_3Si_8N_{11}O_4$ host.

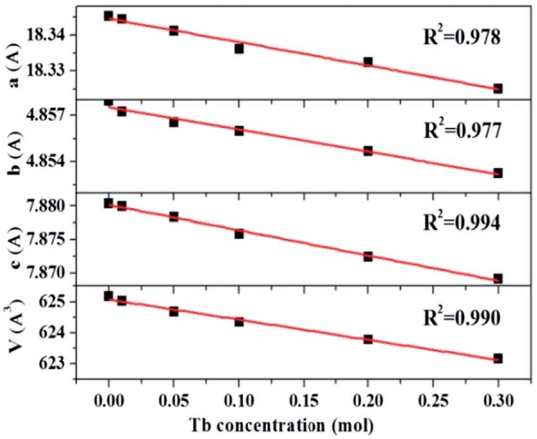

Fig. 2 Lattice parameters (*a*, *b* and *c*) and volume (*V*) of $La_3Si_8N_{11}O_4$:0.01Ce,*x*Tb ($x = 0-0.3$).

when La^{3+} is partially replaced by Ce^{3+} and Tb^{3+} ions, the lattice parameters and the cell volume of the substituted samples will shrink to some extent, which is in line with the reduction of the lattice parameters.

3.2 SEM and TEM

In order to further confirm the composition uniformity of the samples, the SEM and TEM observations of the $La_3Si_8N_{11}O_4$:0.01Ce,0.2Tb phosphor were carried out, as illustrated in Fig. 3 and 4. The elemental mapping images evidence that La, Si, N, O, Ce and Tb are homogeneously distributed within the phosphor particles, which indicates that both Ce and Tb ions are accommodated in the $La_3Si_8N_{11}O_4$ lattice. As seen in Fig. 4a and c, Ce and Tb are distributed uniformly in the sample that is well crystallized. The *d*-spacing of the (11−2) crystal plane is 0.299 and 0.300 nm for $La_3Si_8N_{11}O_4$:0.01Ce,0.2Tb and $La_3Si_8N_{11}O_4$, respectively. It further confirms the successful introduction of Ce^{3+} and Tb^{3+} into the lattice. The ratio of (La + Ce + Tb)/Si is 0.396, which is close to the theoretical ratio of 0.375 (3 : 8), as is shown in Fig. S1.†

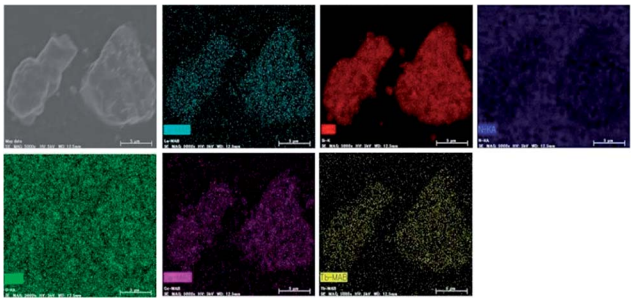

Fig. 3 SEM image and elemental mapping of La, Si, N, O, Ce, and Tb in $La_3Si_8N_{11}O_4$:0.01Ce,0.2Tb.

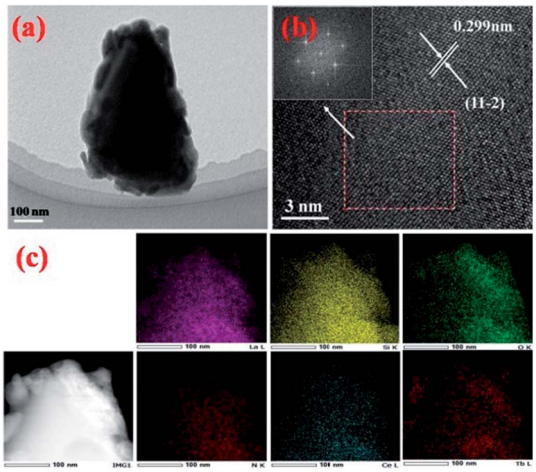

Fig. 4 (a) TEM image, (b) HRTEM images, and (c) elemental mapping of $La_3Si_8N_{11}O_4$:0.01Ce,0.2Tb. The inset of (b) shows the fast Fourier transforms of the HRTEM image.

3.3 Photoluminescence properties

The excitation and emission spectra of single- and co-doped $La_3Si_8N_{11}O_4$ phosphors are descripted in Fig. 5. As seen in Fig. 5a, the PLE spectrum of $La_3Si_8N_{11}O_4$:0.01Ce, monitored by 423 nm, consists of three distinct bands centered at 257, 340, and 360 nm, respectively. The strong PLE band at 340–370 nm matches well with the near-UV LED chip, indicating that the phosphor could be used in white LEDs. Under the 360 nm excitation, the phosphor exhibits a broad asymmetric emission band covering the spectral range of 380–500 nm and a maximum emission at 423 nm. The emission is assigned to the 5d → 4f electronic transitions of Ce^{3+}. The emission band can be divided into two sub-bands centered at 413 nm (24 213 cm^{-1}) and 442 nm (22 624 cm^{-1}) by Gaussian fitting (Fig. 4d). The energy difference between two sub-bands is about 1589 cm^{-1}, which is close to 2000 cm^{-1} (energy difference between $^2F_{7/2}$ and $^2F_{5/2}$ of Ce^{3+}).

Fig. 5b shows the PL and PLE of the single Tb^{3+} doped $La_3Si_8N_{11}O_4$ sample. The emission spectrum consists of several sharp peaks at 489, 543, 580 and 620 nm, which are assigned to the $^5D_4 \rightarrow {}^7F_J$ ($J = 6, 5, 4, 3$) transitions of Tb^{3+}, respectively. The excitation spectrum is composed of a strong broad band spanning 200 to 400 nm, and has a maximum at 284 nm and a weak

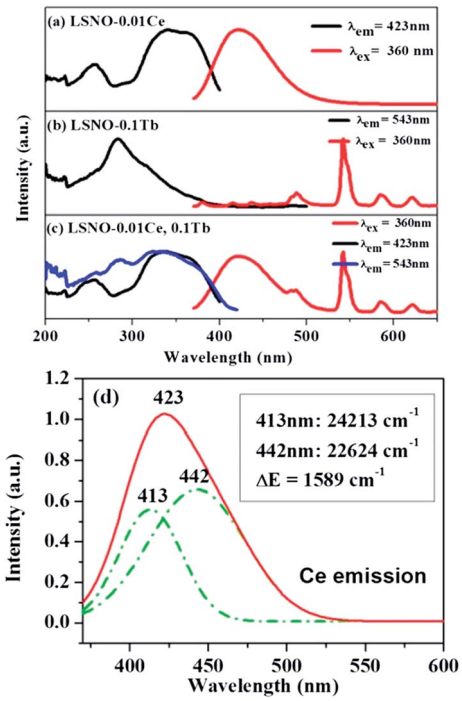

Fig. 5 PL and PLE of (a) $La_3Si_8N_{11}O_4$:0.01Ce, (b) $La_3Si_8N_{11}O_4$:0.05Tb and (c) $La_3Si_8N_{11}O_4$:0.01Ce,0.05Tb, and (d) Gaussian splitting of the emission spectrum of $La_3Si_8N_{11}O_4$:0.01Ce.

band at ~480 nm. It corresponds to the f–f electronic transitions of Tb^{3+}. It is clearly shown that there is a great spectral overlap between the emission band of Ce^{3+} and the excitation band of Tb^{3+}, which indicates the possibility of energy transfer from Ce^{3+} (sensitizer) to Tb^{3+} (activator) according to the Dexter theory.[58]

To confirm the energy transfer between Ce^{3+} and Tb^{3+} in $La_3Si_8N_{11}O_4$, the photoluminescence properties of the co-doped samples were investigated, as shown in Fig. 5c. Clearly, the PLE spectrum monitored at 543 nm of Tb^{3+} exhibits not only a strong absorption band of Tb^{3+} in the range of 260–300 nm, but also contains a characteristic excitation band of Ce^{3+} in the spectral range of 300–400 nm. Additionally, the stronger Tb^{3+} emission appears under the excitation at 360 nm in the co-doped sample. It implies that the energy transfer from Ce to Tb occurs, and the emission of Tb^{3+} is significantly enhanced under the near-UV excitation (*i.e.*, 360 nm).

3.4 Cathodoluminescence (CL) spectra and mapping

Compared to PL with the weak excitation energy (photon: 0.5–6 eV), CL has the stronger excitation source (e-beam: 2–300 keV), which thus enables to provide the information of localized luminescence. As shown in Fig. 6, the CL images of $La_3Si_8N_{11}O_4$:0.01Ce,0.20 Tb, taken at 418 nm (Ce^{3+}) and 544 nm (Tb^{3+}), are quite similar. It indicates that both the Ce^{3+} and Tb^{3+} emissions are from the same host lattice. Furthermore, with increasing x value from 0 to 0.20, the 418 nm emission decreases (from 2.01×10^5 to 1.52×10^5 cps), while the 544 nm emission increases (from 0 to 0.58×10^5 cps). This is an evidence of the energy transfer from Ce^{3+} to Tb^{3+}.

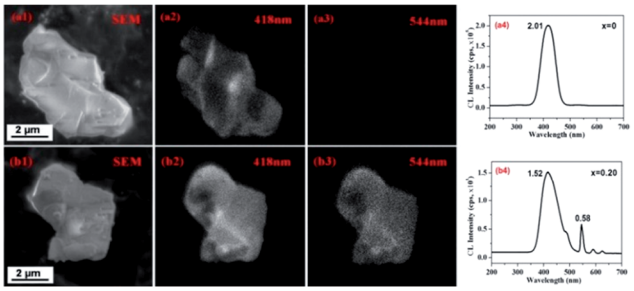

Fig. 6 SEM images (a1 and b1), CL images taken at 418 nm (a2 and b2) and 544 nm (a3 and b3) and CL spectra (a4 and b4) of $La_3Si_8N_{11}O_4$:0.01Ce and $La_3Si_8N_{11}O_4$:0.01Ce,0.20 Tb.

3.5 Energy transfer mechanism

Fig. 7 shows the emission spectra of $La_3Si_8N_{11}O_4$:0.01Ce,xTb with varying Tb^{3+} concentrations ($x = 0$–0.3) under the 360 nm excitation. The PL intensity of Ce^{3+} decreases whereas the luminescence of Tb^{3+} at 543 nm increases, which intuitively supports the occurrence of the energy transfer from Ce^{3+} to Tb^{3+}. The energy transfer efficiency (η_T) can be computed by the following equation:[51]

$$\eta_T = 1 - I/I_0$$

where I_0 and I are the emission peak intensity of Ce^{3+} in the absence and presence of Tb^{3+}, respectively. With increasing the Tb^{3+} doping concentration, the energy transfer efficiency increases and reaches the maximum of 59.1% when the Tb^{3+} concentration is 0.30, as shown in Fig. 7b.

The change of the fluorescence decay time is used to further verify the energy transfer from Ce^{3+} to Tb^{3+} in the $La_3Si_8N_{11}O_4$:0.01Ce,xTb sample. The decay time of the 423 nm emission of Ce^{3+} nearly keeps unchanged with increasing the Tb^{3+} concentration, which is different from the change in peak emission intensity, as shown in Fig. 8. The reason for the unobvious change of lifetime and the decrease of emission intensity is that, the energy transfer rate is faster than the radiative transfer rate in the process of the electronic transitions of 5d → 4f of Ce^{3+} ions, and the fast energy transfer rate

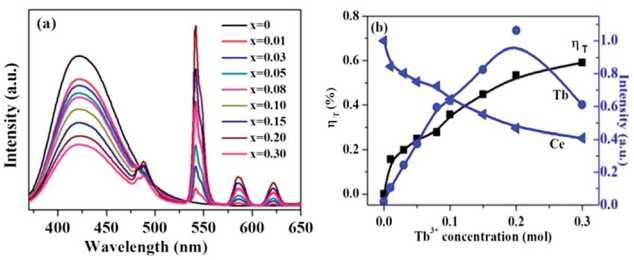

Fig. 7 (a) PL spectra of $La_3Si_8N_{11}O_4$:0.01Ce,xTb with varying Tb^{3+} concentrations ($x = 0$–0.3) under 360 nm excitation, and (b) the normalized peak intensity of the Tb^{3+} emission at 543 nm and the Ce^{3+} emission at 423 nm, and the energy transfer efficiency η_T as a function of the Tb concentration.

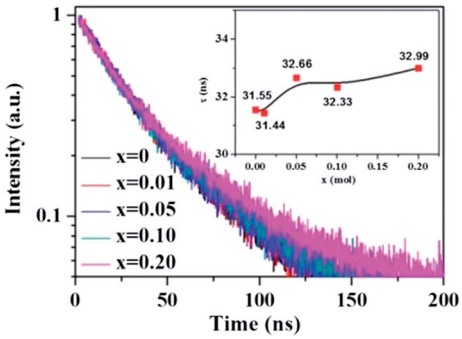

Fig. 8 Fluorescence decay curves and decay times of Ce^{3+} in $La_3Si_8N_{11}O_4$:0.01Ce,*x*Tb under 370 nm excitation and monitored at 423 nm.

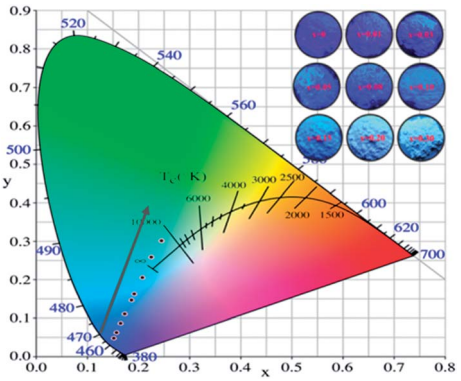

Fig. 10 CIE chromaticity coordinates and the color of $La_3Si_8N_{11}O_4$:0.01Ce,*x*Tb phosphors under the 365 nm irradiation.

can quench the emission intensity while not affect the life time. It is also true in the $Ba_2Y_5B_5O_{17}$:Ce,Tb phosphor.[30]

According to the energy transfer theory proposed by Dexter, concentration quenching is due to the energy transfer from one activator to another until an energy sink in the lattice is reached. As put forward by Blasse, the critical distance (R_{Ce-Tb}) between Ce^{3+} and Tb^{3+} ions can be calculated as below:[59]

$$R_{Ce-Tb} = 2[3V/4\pi x_c N]^{1/3}$$

where N is the number of available sites for the dopant in the unit cell, V is the volume of the unit cell, and x_c is the total of the concentration of Ce^{3+} and Tb^{3+} at which the luminescence of Ce^{3+} is half compared to the sample containing no Tb^{3+} ions. In this work, $N = 24$, $V \approx 1272$ Å^3, and $x_c = 0.19$. Thus, the R_{Ce-Tb} distance is calculated to be about 8.07 Å. It is well known that if the critical distance between sensitizer and activator is much bigger than 4 Å, the energy transfer from Ce^{3+} and Tb^{3+} mainly takes place *via* multipolar interaction rather than exchange interaction.[60] On the basis of the Dexter's energy transfer expression of multipolar interaction and Reisfeld's approximation, the following equation can be given as:[60]

$$I_0/I \propto C^{n/3}$$

where C is the sum of the content of Ce^{3+} and Tb^{3+}. The plots of (I_0/I) *versus* $C^{n/3}$ with $n = 6$, 8, and 10 correspond to dipole–dipole, dipole-quadrupole, and quadrupole–quadrupole interactions, respectively. Fig. 9 illustrates the relationships between (I_0/I) *versus* C. A linear relationship is well fitted at $n = 6$, which clearly indicates that the energy transfer mechanism is dipole–dipole interaction.

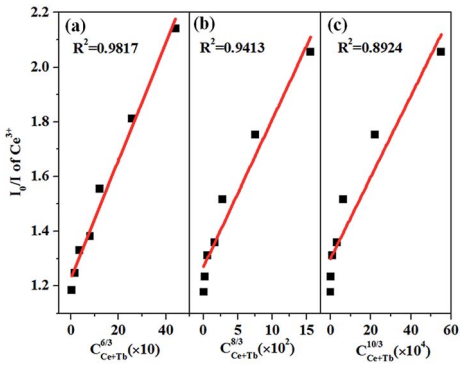

Fig. 9 Dependence of I_0/I of Ce^{3+} on (a) $C^{n/3}$, (b) $C^{n/3}$, and (c) $C^{n/3}$.

The Commission International de I'Eclairage (CIE) 1931 chromaticity coordinates of the $La_3Si_8N_{11}O_4$:0.01Ce,*x*Tb were calculated, as shown in Fig. 10. The color can be changed from blue (0.1523, 0.0483) at $x = 0$ to green (0.2455, 0.3013) at $x = 0.3$. The green emission of Tb^{3+} dominates the luminescence when x is up to 0.1, which could be used as a potential green-emitting phosphor in near-UV LED driven white LEDs.

3.6 Quantum efficiency

The absorption, internal and external quantum (IQE and EQE) efficiencies of single- and co-doped $La_3Si_8N_{11}O_4$:Ce,Tb samples under different wavelength excitations are shown in Fig. 11. Due to the stronger absorption in co-doped sample, the absorption, IQE and EQE of the $La_3Si_8N_{11}O_4$:0.01Ce,0.05Tb under 360 nm excitation are about 55, 76.3 and 46.7%, while those of $La_3Si_8N_{11}O_4$:0.05Tb are about 11, 77.7 and 8.3%, respectively. The PL intensity of Tb^{3+} is improved by about 9 times under 360 nm excitation due to the strong energy transfer from Ce^{3+} to Tb^{3+}, as shown in Fig. 12.

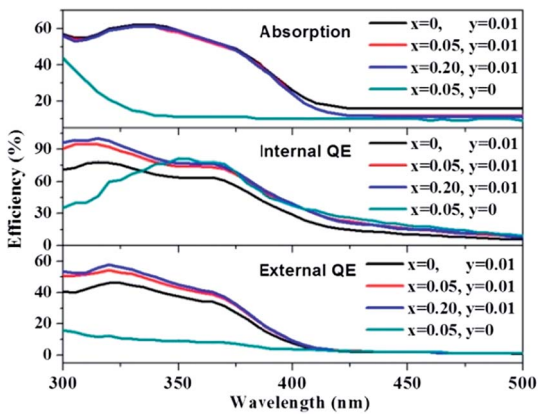

Fig. 11 Absorption, quantum efficiency of $La_3Si_8N_{11}O_4$:0.01Ce,*x*Tb (x = 0, 0.05, 0.20) and $La_3Si_8N_{11}O_4$:*y*Ce,*x*Tb ($y = 0$, $x = 0.05$).

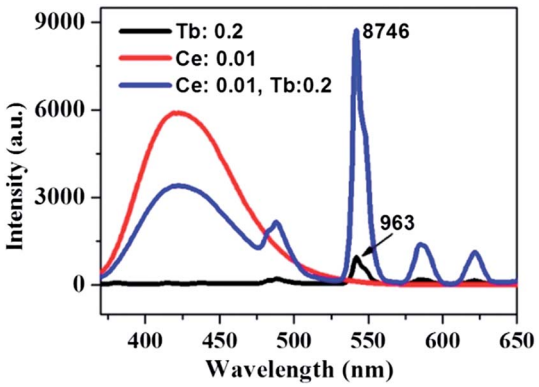

Fig. 12 PL spectra of $La_3Si_8N_{11}O_4$:0.2Tb, $La_3Si_8N_{11}O_4$:0.01Ce and $La_3Si_8N_{11}O_4$:0.01Ce,0.2Tb under the 360 nm excitation.

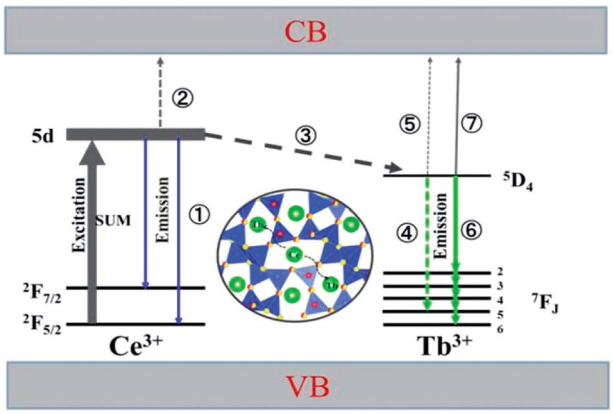

Fig. 14 The model of the $Ce^{3+} \rightarrow Tb^{3+}$ energy transfer and the emission processes of $Ce^{3+}$and Tb^{3+}.

3.7 Thermal quenching

Thermal stability of a phosphor is an indispensable factor that cannot be neglected for its application in white LEDs. Fig. 13 shows the temperature-dependent luminescence of the Ce-, Tb-single doped and co-doped $La_3Si_8N_{11}O_4$ samples under 360 nm excitation. For the Ce^{3+} emission at 423 nm, the thermal quenching is nearly equivalent for both the single- and co-doped samples. On the other hand, for the Tb^{3+} emission, the Ce^{3+}/Tb^{3+} co-doped $La_3Si_8N_{11}O_4$ samples show smaller thermal quenching than either the Ce^{3+}- or the Tb^{3+}-doped sample, which indicates that the energy transfer from Ce^{3+} to Tb^{3+} contributes significantly to the enhanced thermal stability.

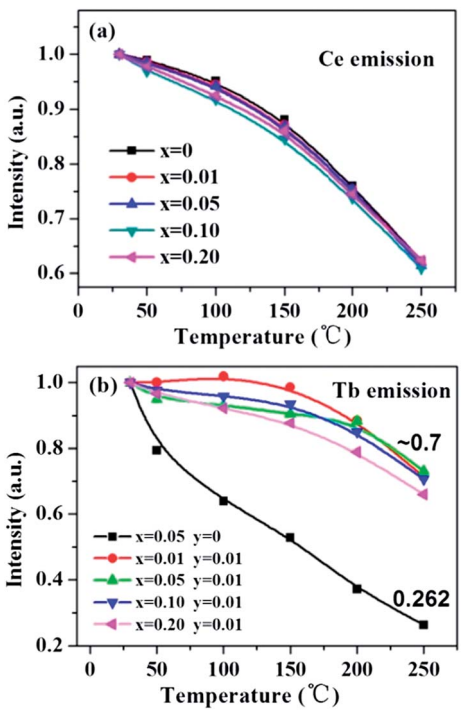

Fig. 13 Temperature dependence of (a) the Ce emission intensity in $La_3Si_8N_{11}O_4$:0.01Ce,*x*Tb and (b) the Tb emission intensity in $La_3Si_8N_{11}O_4$:*y*Ce,*x*Tb ($y = 0$, 0.05).

Based on the thermal activation model, the excited 5d electrons of Ce^{3+} will be mainly involved in three processes, as illustrated in Fig. 14.[30] The first process (1), defined as N_{EM}, is the intrinsic emission electrons of the lowest 5d state of Ce^{3+}. The second process (2), defined as N_{TQ}, is the thermal activation electrons and equal to $Ae^{-\Delta E/kT}$ (A is a constant, ΔE is the activation energy for thermal quenching, and k is Boltzmann constant). And the third process (3), named as N_{ET}, is the energy transfer electrons between Ce^{3+} and Tb^{3+}. Therefore, the energy transfer efficiency (η_{ET}) can be written as:

$$\eta_{ET} = \frac{N_{ET}}{N_{SUM}} = \frac{N_{ET}}{N_{EM} + N_{TQ} + N_{ET}} \quad (1)$$

As the thermal quenching behavior of the Ce^{3+} luminescence of the single- and co-doped samples is almost the same, the luminescence of Ce^{3+} changes very little at a certain temperature. It indicates that the change in energy transfer rate is mainly attributed to the thermal activation electrons rather than the intrinsic emission electrons when the temperature increases. Therefore, the number of energy transfer electrons increases, which thus contributes to the increased Tb^{3+} luminescence in the co-doped samples.

At the same time, the electrons, coming from the energy transfer of Ce^{3+}, will be separated into process 4 ($N_{EM\text{-}Ce}$) and process 5 ($N_{TQ\text{-}Ce}$), which stands for the intrinsic emission and thermal activation electrons of Tb^{3+}. That is to say, the emission of Tb^{3+} does not contain the intrinsic emission of Tb^{3+} (process 6, $N_{EM\text{-}Tb}$) but it originated from the energy transfer from Ce^{3+}. Therefore, the temperature-dependent luminescence of Tb^{3+} in the single-doped ($\eta_{EM\text{-}S\text{-}Tb}$) and the co-doped sample ($\eta_{EM\text{-}C\text{-}Tb}$) can be calculated by the following equations:

$$\eta_{EM\text{-}S\text{-}Tb} = \frac{N_{EM\text{-}Tb}}{N_{EM\text{-}Tb} + N_{TQ\text{-}Tb}} \quad (2)$$

$$\eta_{EM\text{-}C\text{-}Tb} = \frac{N_{ET}\dfrac{N_{EM\text{-}Ce}}{N_{EM\text{-}Ce} + N_{TQ\text{-}Ce}} + N_{EM\text{-}Tb}}{N_{ET} + N_{EM\text{-}Tb} + N_{TQ\text{-}Tb}} \quad (3)$$

where $N_{TQ\text{-}Tb}$ is the thermal activation electrons of the intrinsic Tb^{3+}. For the co-doped phosphor, we may infer that the electrons coming from the energy transfer of Ce^{3+} mainly contribute to the emission rather than thermal activation, and the emission of Tb^{3+} hence shows a higher thermal stability. If $N_{EM\text{-}Ce}$ is smaller than $N_{TQ\text{-}Ce}$, the emission of Tb^{3+} would exhibit a lower thermal stability than that in the single-doped sample.

Additionally, as the temperature increases from 30 to 250 °C, the CIE chromaticity coordinates of $La_3Si_8N_{11}O_4$:0.01Ce,0.20Tb show a small variation (Fig. 15). Compared to the CIE x value, the CIE y value has a greater change. It is mainly due to the increasing ratio of the Tb^{3+} emission intensity to the Ce^{3+} one. This agrees well with the faster quenching of the Ce^{3+} emission with increasing the temperature, as discussed above.

As aforementioned, the temperature-dependent luminescence of Tb^{3+} ($\eta_{EM\text{-}C\text{-}Tb}$) will be enhanced owing to the increased number of electrons from Ce^{3+}(N_{ET}) *via* the energy transfer. As seen in Fig. 16, the emission intensity of Tb^{3+} in $La_3Si_8N_{11}O_4$:yCe, 0.05Tb (y = 0–0.20) samples is enhanced as the Ce^{3+} concentration increases. It indicates that the higher Ce^{3+} concentration generates more electrons that are transferred to Tb^{3+}, which is well accordance with the analysis from eqn (1) and (3). Moreover, the change of the decay time of $La_3Si_8N_{11}O_4$:yCe,0.05Tb (y = 0–0.20) also provides the evidence that more electrons are transferred from Ce^{3+} to Tb^{3+} with increasing the Ce^{3+} concentration, as shown in Fig. 17. In addition, as shown in Fig. 18, the thermal quenching of the Tb^{3+} emission in the co-doped $La_3Si_8N_{11}O_4$:yCe,0.05Tb (y = 0–0.20) samples is smaller than that in the single-doped sample. When the Ce^{3+} concentration increases, the thermal stability of the Tb^{3+} emission gradually enhances. At 200 °C, the emission intensity of the single-doped sample ($La_3Si_8N_{11}O_4$:0.05Tb) declines by 63%, whereas it losses only by 10% in the co-doped samples ($La_3Si_8N_{11}O_4$:yCe,0.05Tb, y = 0.01–0.10). The small reduction in luminescence of Tb^{3+} in the co-doped samples implies that the energy transfer from Ce^{3+} to Tb^{3+} dominantly contributes to the emission of Tb^{3+}. The thermal quenching of the sample at y = 0.15 becomes much larger than others, which may be due to the increased lattice distortion caused by the substitution of La by Ce and Tb.

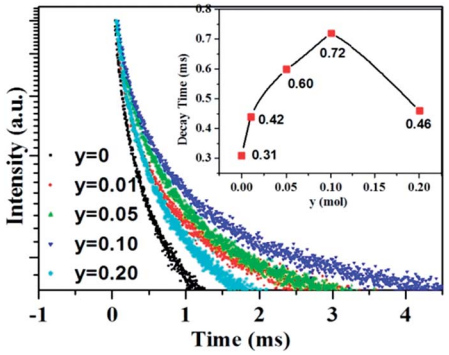

Fig. 17 Luminescence decay curves of the $La_3Si_8N_{11}O_4$:yCe,0.05Tb (y = 0–0.20) samples under 370 nm excitation, monitored by the peak wavelength of Tb^{3+} (544 nm).

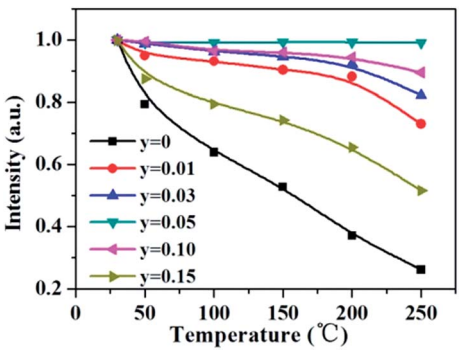

Fig. 18 Temperature dependence of the Tb^{3+} emission intensity in $La_3Si_8N_{11}O_4$:yCe,0.05Tb (y = 0–0.15) under the 360 nm excitation.

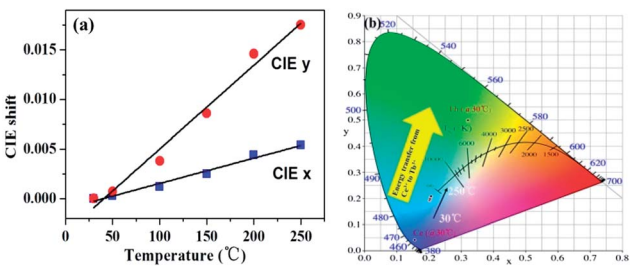

Fig. 15 Temperature-dependent (a) CIE chromaticity coordinates and (b) the color point shift of $La_3Si_8N_{11}O_4$:0.01Ce,0.20Tb sample.

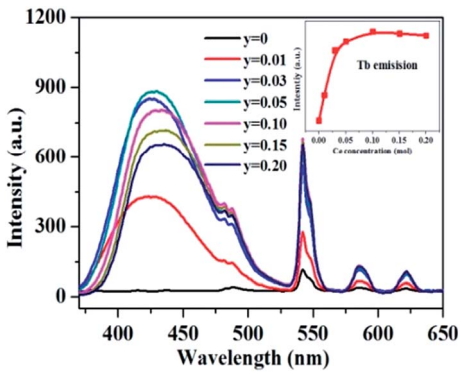

Fig. 16 PL spectra and the peak intensity of Tb^{3+} emission under 360 nm excitation in the $La_3Si_8N_{11}O_4$:yCe,0.05Tb (y = 0–0.15) samples.

3.8 Applications in white LEDs

In order to testify the suitability of the blue-green $La_3Si_8N_{11}O_4$:0.01Ce,0.05Tb phosphor in white LEDs, it was mixed with $SrSi_2N_2O_2$:Eu (green) and $Sr_2Si_5N_8$:Eu (red) phosphors to form a phosphor blend, and then pumped by a UV-LED chip (365 nm). As seen in Fig. 19, the white LED has the chromaticity coordinates of x = 0.391, y = 0.361, a correlated color temperature (CCT) of 3570 K and a high color rendering index (CRI) of 90.2. The luminous efficiency of this white LED is as low as 4.4 lm W^{-1}, which is mainly due to the low efficiency of the UV-LED

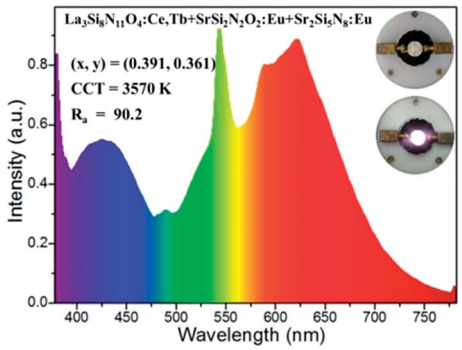

Fig. 19 The electroluminescence spectrum of the white LED using a UV-LED chip (365 nm) and $La_3Si_8N_{11}O_4$:0.01Ce,0.05Tb, $SrSi_2N_2O_2$:Eu and $Sr_2Si_5N_8$:Eu phosphors. The inset shows images of the white LED (power off and on).

chip (0.78 lm W^{-1}). These results demonstrate that the title phosphor could be a promising blue-green phosphor for use in UV-LED driven white LEDs.

4 Conclusions

The energy transfer between Ce^{3+} and Tb^{3+} was realized in the co-doped $La_3Si_8N_{11}O_4$ phosphors. The emission color could be tuned from blue (Ce^{3+}) to green (Tb^{3+}) under the 360 nm excitation, and the Tb^{3+} luminescence of the co-doped sample was improved by 9 times owing to the energy transfer of $Ce^{3+} \rightarrow Tb^{3+}$. The external quantum efficiency of $La_3Si_8N_{11}O_4$:0.01Ce,0.05Tb was 46.7% under the 360 nm excitation, which is much higher than that of 8.3% for $La_3Si_8N_{11}O_4$:0.05Tb. The thermal quenching of the co-doped samples was significantly reduced, with the luminescence loss of Tb^{3+} emission decreasing from 74 to 30% at 250 °C. A UV-LED driven white LED using $La_3Si_8N_{11}O_4$:0.01Ce,0.05Tb, $SrSi_2N_2O_2$:Eu and $Sr_2Si_5N_8$:Eu phosphors was fabricated, and it had a correlated color temperature of 3570 K, a high color rendering index of 90.2, and a luminous efficacy of 4.4 lm W^{-1}. It indicates that the Ce^{3+}/Tb^{3+} co-doped $La_3Si_8N_{11}O_4$ ($La_3Si_8N_{11}O_4$:0.01Ce,0.05Tb) would be an interesting blue-green phosphor for UV LEDs.

Conflicts of interest

There are no conflicts to declare.

Acknowledgements

We are grateful for the National Nature Science Foundation of China (No. 51502020, 5157223, and 51561135015), the National Basic Research Program of China (No. 2014CB643801), and the National Key Research and Development program (No. 2017YFB0404301).

Notes and references

1 R.-J. Xie, N. Hirosaki, N. Kimura, K. Sakuma and M. Mitomo, *Appl. Phys. Lett.*, 2007, **90**, 191101.
2 Z.-G. Xia and A. Meijerink, *Chem. Soc. Rev.*, 2017, **46**(1), 275–299.
3 H.-B. Xu, W.-D. Zhuang, L. Wang, R.-H. Liu, Y.-H. Liu, L.-H. Liu, Y. Cho, N. Hirosaki and R.-J. Xie, *Inorg. Chem.*, 2017, **56**, 14170–14177.
4 S. H. Lim, Y. H. Ko, C. Rodriguez, S. H. Gong and Y. H. Cho, *Light: Sci. Appl.*, 2016, **5**(2), 16030.
5 W. Lu, J. Huo, Y. Feng, S. Zhao and H. You, *Dalton Trans.*, 2016, **45**, 9676–9683.
6 P.-P. Dai, C. Li, X.-T. Zhang, J. Xu, X. Chen, X.-L. Wang, Y. Jia, X.-J. Wang and Y.-C. Liu, *Light: Sci. Appl.*, 2016, **5**(2), 16024.
7 P. Pust, V. Weiler, C. Hecht, A. Tucks, A. S. Wochnik, A. K. Henß, D. Wiechert, C. Scheu, P. J. Schmidt and W. Schnick, *Nat. Mater.*, 2014, **13**, 891–896.
8 N. Hirosaki, T. Takeda, S. Funahashi and R.-J. Xie, *Chem. Mater.*, 2014, **26**, 4280–4288.
9 M. Zeuner, S. Pagano and W. Schnick, *Angew. Chem., Int. Ed.*, 2011, **50**, 7754–7775.
10 R.-J. Xie and H. T. Bert Hintzen, *J. Am. Ceram. Soc.*, 2013, **96**, 665–687.
11 S. Schmiechen, H. Schneider, P. Wagatha, C. Hecht, P. J. Schmidt and W. Schnick, *Chem. Mater.*, 2014, **26**, 2712–2719.
12 Y.-H. Liu, X.-F. Zhou, L. Chen, W.-D. Zhuang, R.-H. Liu and Y.-S. Hu, *J. Rare Earths*, 2017, **35**(3), 223–229.
13 T. Takeda, N. Hirosaki, S. Funahshi and R.-J. Xie, *Chem. Mater.*, 2015, **27**, 5892–5898.
14 R.-J. Xie, N. Hirosaki and T. Takeda, *Appl. Phys. Express*, 2009, **2**, 022401.
15 H.-P. Ji, L. Wang, M. S. Molokeev, N. Hirosaki, Z.-H. Huang, Z.-G. Xia, O. M. Kate, L.-H. Liu and R.-J. Xie, *J. Mater. Chem. C*, 2016, **4**, 2359–2366.
16 S.-S. Liang, M.-M. Shang, H.-Z. Lian, K. Li, Y. Zhang and J. Lin, *J. Mater. Chem. C*, 2017, **5**, 2927–2935.
17 W.-T. Chen, H. S. Sheu, R.-S. Liu and J. P. Attfield, *J. Am. Chem. Soc.*, 2012, **134**, 8022–8025.
18 W. Lü, H.-W. Xu, J.-S. Huo, B.-Q. Shao, Y. Feng, S. Zhao and H.-P. You, *Dalton Trans.*, 2017, **46**, 9272–9279.
19 W.-R. Zhao, W.-D. Zhuang, F. Du, Y.-N. Zhou, Y.-L. Yu and L.-G. Wang, *J. Alloys Compd.*, 2017, **726**, 658–663.
20 Y. Chen, F.-J. Pan, M. Wang, X.-J. Zhang, J. Wang, M.-M. Wu and C.-X. Wang, *J. Mater. Chem. C*, 2016, **4**, 2367–2373.
21 K. Takahashi, N. Hirosaki, R.-J. Xie, M. Harade, K. Yoshimura and Y. Tomomura, *Appl. Phys. Lett.*, 2007, **91**, 091923.
22 B. Dierre, R.-J. Xie, N. Hirosaki and T. Sekiguchi, *J. Mater. Res.*, 2007, **22**(7), 1933–1941.
23 C.-C. Lin, W.-T. Chen, C.-I. Chu, K.-W. Huang, C. W. Yeh, B.-M. Cheng and R.-S. Liu, *Light: Sci. Appl.*, 2016, **5**(4), 16066.
24 X.-Y. Fu, S.-H. Zheng, J.-P. Shi, Y.-C. Li and H.-W. Zhang, *J. Lumin.*, 2017, **184**, 199–204.
25 M.-M. Shang, S.-S. Liang, H.-Z. Lian and J. Lin, *Inorg. Chem.*, 2017, **56**, 6131–6140.
26 Z.-G. Xia and R.-S. Liu, *J. Phys. Chem. C*, 2012, **116**, 15604–15609.
27 J. S. Kim, P. E. Jeon, Y. H. Park, J. C. Choi, H. L. Park, G. C. Kim and T. W. Kim, *Appl. Phys. Lett.*, 2004, **85**, 3696.

28 D.-L. Geng, M.-M. Shang, Y. Zhang, H.-Z. Lian and J. Lin, *Inorg. Chem.*, 2013, **52**, 13708–13718.
29 G. Li, Y.-H. Wang, W. Zeng, W.-B. Chen, S.-C. Han, H.-J. Guo and Y.-Y. Li, *J. Mater. Chem. C*, 2016, **4**(15), 3304–3312.
30 Y. Xiao, Z.-D. Hao, L.-L. Zhang, W.-G. Xiao, D. Wu, X. Zhang, G.-H. Pan, Y.-S. Luo and J.-H. Zhang, *Inorg. Chem.*, 2017, **56**, 4538–4544.
31 F. Du, W.-D. Zhuang, R.-H. Liu, Y.-H. Liu, J.-Y. Zhong, P. Gao, X. Zhang, W. Gao and L.-L. Shao, *RSC Adv.*, 2017, **7**, 1075–1081.
32 X. G. Zhang, Y.-M. Huang and M.-L. Gong, *J. Chem. Eng.*, 2017, **307**, 291–299.
33 L. Wang, R.-J. Xie, T. Suehiro, T. Takeda and N. Hirosaki, *Chem. Rev.*, 2018, **118**, 1951–2009.
34 Y. Q. Li, J. E. J. van Steen, J. W. H. van Krevel, G. Botty, A. C. A. Delsing, F. J. DiSalvo, G. de With and H. T. Hintzen, *J. Alloys Compd.*, 2006, **417**, 273–279.
35 C.-J. Duan, X.-J. Wang, W. M. Otten, A. C. A. Delsing, J.-T. Zhao and H. T. Hintzen, *Chem. Mater.*, 2008, **20**, 1597–1605.
36 Y.-Q. Li, G. de With and H. T. Hintzen, *J. Alloys Compd.*, 2004, **385**, 1–11.
37 C. Hecht, F. Stadler, P. Schmidt, W. Schnick, J. S. auf der Günne and V. Baumann, *Chem. Mater.*, 2009, **21**, 1595–1601.
38 Y.-Q. Li, A. C. A. Delsing, G. de With and H. T. Hintzen, *Chem. Mater.*, 2005, **17**, 3242–3248.
39 J.-Y. Tang, J.-H. Chen, L.-Y. Hao, X. Xu, W.-J. Xie and Q.-X. Li, *J. Lumin.*, 2011, **131**, 1101–1106.
40 O. Oeckler, J. A. Kechele, H. Koss, P. J. Schmidt and W. Schnick, *Chem.–Eur. J.*, 2009, **15**, 5311–5319.
41 Y. Fukuda, K. Ishida, I. Mitsuishi and S. Nunoue, *Appl. Phys. Express*, 2009, **2**, 012401.
42 J. Grins, S. Esmaeilzadeh, G. Svensson and Z. J. Shen, *J. Eur. Ceram. Soc.*, 1999, **19**, 2723–2730.
43 X.-J. Wang, L. Wang, T. Takeda, S. Funahashi, T. Suehiro, N. Hirosaki and R.-J. Xie, *Chem. Mater.*, 2015, **27**, 7689–7697.
44 W. B. Park, S. P. Singh, C. Yoon and K. S. Sohn, *J. Mater. Chem.*, 2012, **22**, 14068–14075.
45 X.-J. Wang, S. Funahashi, T. Takeda, T. Suehiro, N. Hirosaki and R.-J. Xie, *J. Mater. Chem. C*, 2016, **4**, 9968–9975.
46 R.-J. Xie, N. Hirosaki, M. Mitomo, Y. Yamamoto, T. Suehiro and N. Ohashi, *J. Am. Ceram. Soc.*, 2004, **87**, 1368–1370.
47 N. Hirosaki, R.-J. Xie and K. Kimoto, *Appl. Phys. Lett.*, 2005, **86**, 211905.
48 K. Uheda, N. Hirosaki, Y. Yamamoto, A. Naito, T. Nakajima and H. Yamamoto, *Electrochem. Solid-State Lett.*, 2006, **9**, 22–25.
49 P. Pust, V. Weiler, C. Hecht, A. Tücks, A. S. Wochnik, A. K. Henß, D. Wiechert, C. Scheu, P. J. Schmidt and W. Schnick, *Nat. Mater.*, 2014, **13**, 891–896.
50 T. Seto, N. Kijima and N. Hirosaki, *ECS Trans.*, 2009, **25**, 247–252.
51 L.-H. Liu, L. Wang, C.-N. Zhang, Y. Cho, B. Dierre, N. Hirosaki, H. Sekiguchi and R.-J. Xie, *Inorg. Chem.*, 2015, **54**(11), 5556–5565.
52 X.-F. Song, R.-L. Fu, S. Agathopoulos, H. He, X.-R. Zhao and R. Li, *J. Electrochem. Soc.*, 2010, **157**, 34–38.
53 C.-Y. Wang, T. Takeda, O. M. ten Kate, M. Tansho, K. Deguchi, K. Takahashi, R.-J. Xie, T. Shimizu and N. Hirosaki, *ACS Appl. Mater. Interfaces*, 2017, **9**(27), 22665–22675.
54 B. Dierre, R.-J. Xie, N. Hirosaki and T. Sekiguchi, *J. Mater. Res.*, 2007, **22**(7), 1933–1941.
55 K. Ohkubo and T. J. Shigeta, *Journal of the Illuminating Engineering Institute of Japan*, 1999, **83**, 87.
56 J. Grins, Z. Shen, S. Esmaeilzadeh and P. Berastegui, *J. Mater. Chem.*, 2001, **11**, 2358–2362.
57 R. D. Shannon, *Acta Crystallogr.*, 1976, **32**, 751–767.
58 D. L. Dexter, *J. Chem. Phys.*, 1953, **21**, 836–850.
59 G. Blass, *Philips Res. Rep.*, 1969, **24**, 131.
60 D. L. Dexter and J. A. Schulaman, *J. Chem. Phys.*, 1954, **22**, 1063–1070.